

Article

Iron-Based Composite Oxide Catalysts Tuned by CTAB Exhibit Superior NH₃–SCR Performance

Wenshuo Zhang^{1,2}, Xiaoyan Shi^{1,2}, Meng Gao^{1,2}, Jingjing Liu¹, Zhihui Lv^{1,2}, Yingjie Wang³, Yanlong Huo^{1,2}, Chang Cui^{1,2}, Yunbo Yu^{1,2,3,4,*} and Hong He^{1,2,4,*}

- ¹ State Key Joint Laboratory of Environment Simulation and Pollution Control, Research Center for Eco-Environmental Sciences, Chinese Academy of Sciences, Beijing 100085, China; wszhang_st@rcees.ac.cn (W.Z.); xyshi@rcees.ac.cn (X.S.); menggao_st@rcees.ac.cn (M.G.); jlliu@rcees.ac.cn (J.L.); zhlv_st@rcees.ac.cn (Z.L.); yluo_st@rcees.ac.cn (Y.H.); changcui_st@rcees.ac.cn (C.C.)
- ² University of Chinese Academy of Sciences, Beijing 100049, China
- ³ Ganjiang Innovation Academy, Chinese Academy of Sciences, Ganzhou 341000, China; yjwang@ire.ac.cn
- ⁴ Center for Excellence in Regional Atmospheric Environment, Institute of Urban Environment, Chinese Academy of Sciences, Xiamen 361021, China
- * Correspondence: ybyu@rcees.ac.cn (Y.Y.); honghe@rcees.ac.cn (H.H.)

Abstract: Iron-based oxide catalysts for the NH₃–SCR (selective catalytic reduction of NO_x by NH₃) reaction have gained attention due to their high catalytic activity and structural adjustability. In this work, iron–niobium, iron–titanate and iron–molybdenum composite oxides were synthesized by a co-precipitation method with or without the assistance of hexadecyl trimethyl ammonium bromide (CTAB). The catalysts synthesized with the assistance of CTAB (FeM_{0.3}O_x-C, M = Nb, Ti, Mo) showed superior SCR performance in an operating temperature range from 150 °C to 400 °C compared to those without CTAB addition (FeM_{0.3}O_x, M = Nb, Ti, Mo). To reveal such enhancement, the catalysts were characterized by N₂-physisorption, XRD (Powder X-ray diffraction), NH₃-TPD (temperature-programmed desorption of ammonia), DRIFTS (Diffuse Reflectance Infrared Fourier Transform Spectroscopy), XPS (X-ray Photoelectron Spectroscopy), and H₂-TPR (H₂-Total Physical Response). It was found that the crystalline phase of Fe₂O₃ formed was influenced by the presence of CTAB in the preparation process, which favored the formation of crystalline γ -Fe₂O₃. Owing to the changed structure, the redox-acid properties of FeM_{0.3}O_x-C catalysts were modified, with higher exposure of acid sites and improved ability of NO oxidation to NO₂ at low-temperature, both of which also contributed to the improvement of NO_x conversion. In addition, the weakened redox ability of Fe prevented the over-oxidation of NH₃, thus accounting for the greatly improved high-temperature activity as well as N₂ selectivity.

Keywords: NH₃–SCR; selective catalytic reduction; iron-based catalysts; NO_x abatement



Citation: Zhang, W.; Shi, X.; Gao, M.; Liu, J.; Lv, Z.; Wang, Y.; Huo, Y.; Cui, C.; Yu, Y.; He, H. Iron-Based Composite Oxide Catalysts Tuned by CTAB Exhibit Superior NH₃–SCR Performance. *Catalysts* **2021**, *11*, 224. <https://doi.org/10.3390/catal11020224>

Academic Editors: Fabio Alessandro Deorsola and Lidia Castoldi

Received: 19 January 2021
Accepted: 5 February 2021
Published: 8 February 2021

Publisher's Note: MDPI stays neutral with regard to jurisdictional claims in published maps and institutional affiliations.



Copyright: © 2021 by the authors. Licensee MDPI, Basel, Switzerland. This article is an open access article distributed under the terms and conditions of the Creative Commons Attribution (CC BY) license (<https://creativecommons.org/licenses/by/4.0/>).

1. Introduction

Selective catalytic reduction of NO_x by NH₃ (NH₃–SCR) is an effective means of NO_x abatement. Various catalysts have been developed for NH₃–SCR, including metal oxide catalysts (VO_x-based, CeO₂-based, Fe₂O₃-based, MnO_x-based catalysts, etc.) and zeolite catalysts (Cu- and Fe-exchanged zeolite catalysts, etc.) [1,2]. Among them, iron-based oxide catalysts have received much attention due to their high catalytic activity as well as non-toxicity, low cost, and accessibility [1,3,4]. As for NH₃–SCR catalysts, both acid sites and redox sites are necessary to guarantee efficient NO_x reduction [1,5]. High dispersion of sites having the same function and close coupling of redox-acid sites are important for the design of catalysts with superior NH₃–SCR performance [2]. Taking this principle into account, large numbers of iron-based composite oxide catalysts have been prepared and investigated for NH₃–SCR, including Fe–Ti [6–8], Fe–Mo [9–11], Fe–W [12–14], Fe–Nb [15], and so on, in which the Fe component provides redox sites while a second component

supplies acid sites. For instance, Liu et al. [6,16] reported a novel iron titanate catalyst with outstanding performance in the medium-temperature range (200–400 °C), in which a specific Fe–O–Ti structure acted as the main active phase. Recently, Qu et al. [11] identified a di-nuclear entity (an isolated Mo ion and one adjacent surface Fe ion) as the active site in a Mo₁/Fe₂O₃ single-atom catalyst, thus giving an explanation for the improved SCR reaction at acid-redox interfaces.

For iron-based oxides, generally, the γ -Fe₂O₃ crystalline phase shows better activity than α -Fe₂O₃ in NH₃-SCR [7,17,18] and other catalytic reactions, such as CO₂ hydrogenation, photodecomposition of H₂S, and NO reduction by CO [19–21]. However, the γ -Fe₂O₃ active phase is thermally unstable and undergoes irreversible transformation to α -Fe₂O₃ at elevated temperatures. Such transformation generally occurs between 300 °C and 400 °C [18,22–24], related to several factors, including the particle size, morphology of γ -Fe₂O₃ and presence of a coating layer or dopants [23,25]. As a result, maintaining the γ -Fe₂O₃ active phase in iron-based oxide catalysts is of great importance to the durability of catalysts in the NH₃-SCR reaction. To restrain such phase transformation, previous researchers found it effective to introduce another metal into iron oxides, such as Mn, Ti or W, or to fabricate coating layers [21,22,24,26–28].

Hexadecyl trimethyl ammonium bromide (CTAB) is a kind of amphiphilic organic compound containing both hydrophobic and hydrophilic ends [29], which are often used as template-directing agents that can function as both “structural” and “chemical” promoters. It was reported that CTAB could adjust the crystalline phase of metal oxides [30–32]; for instance, the steric hindrance of CTAB was found to prevent the transition of anatase to rutile for TiO₂ [31]. In this study, Nb, Ti and Mo were chosen to couple with Fe in order to provide sufficient acidity for NH₃-SCR [9,18,33–36]. During the preparation process of Fe–M (M = Nb, Ti, Mo) catalysts meanwhile, CTAB was added into the precursor solution. With the assistance of CTAB, the obtained FeM_{0.3}O_x-C catalysts showed much better SCR performance than unassisted FeM_{0.3}O_x catalysts. It was identified that CTAB adjusted the structural properties, contributing to the formation of the γ -Fe₂O₃ phase. Further investigation revealed that the modified catalysts showed high exposure of acid sites and an enhanced ability for low-temperature NO oxidation, but restrained behavior for NH₃ oxidation at high temperatures, thus contributing to improved NO_x conversion and N₂ selectivity.

2. Results

2.1. NH₃-SCR Performance

The NO_x conversion in the NH₃-SCR reaction over all the prepared catalysts under the high GHSV (gaseous hourly space velocity) of 500,000 h^{−1} is shown in Figure 1. At 150 °C, the NO_x conversion over FeNb_{0.3}O_x-C was 9%, which was slightly higher than that of FeNb_{0.3}O_x (7%). With the rising temperature, the SCR activity of FeNb_{0.3}O_x-C increased significantly, with NO_x conversion of 73% at 300 °C, which was much higher than the value of 54% for FeNb_{0.3}O_x. Such an increase in NO_x conversion was also observed over Fe–Ti and Fe–Mo catalysts, especially at higher temperatures. Meanwhile, FeM_{0.3}O_x-C catalysts showed higher N₂ selectivity than FeM_{0.3}O_x catalysts, as shown in Figure S1.

2.2. Kinetic Studies

The Arrhenius plots of the reaction rates for the reduction of NO_x in the range of 200–320 °C are shown in Figure 2. The apparent activation energies (E_a) were then calculated from the fitted curves and are shown in Table 1. It was noted that the E_a of FeNb_{0.3}O_x-C was 34.5 kJ mol^{−1}, similar to that of FeNb_{0.3}O_x (40.0 kJ mol^{−1}). This was further confirmed by the reaction results of Fe–Ti and Fe–Mo catalysts with similar values of E_a (shown in Table 1). Figure 2 also shows that the three FeM_{0.3}O_x-C catalysts exhibited almost the same reaction rate per square meter of surface area, which is further listed in Table 1 (reaction rate at 260 °C). In agreement with Figure 1, the activities of FeM_{0.3}O_x-C

were higher than those of $\text{FeM}_{0.3}\text{O}_x$. Among the three $\text{FeM}_{0.3}\text{O}_x$ samples, interestingly, $\text{FeTi}_{0.3}\text{O}_x$ and $\text{FeMo}_{0.3}\text{O}_x$ exhibited similar reaction rates.

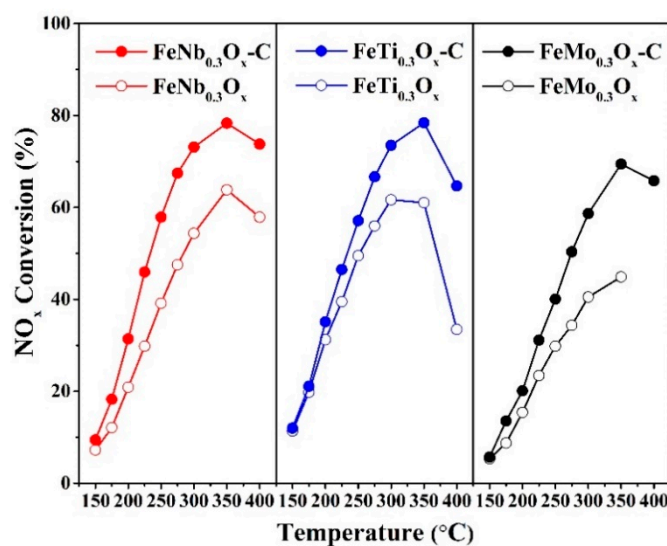


Figure 1. NO_x conversion over all the $\text{FeM}_{0.3}\text{O}_x\text{-C}$ and $\text{FeM}_{0.3}\text{O}_x$ ($M = \text{Nb, Ti, Mo}$) samples. Reaction conditions: $[\text{NO}] = [\text{NH}_3] = 500$ ppm, $[\text{O}_2] = 5$ vol %, N_2 balance, $\text{GHSV} = 500,000$ h^{-1} .

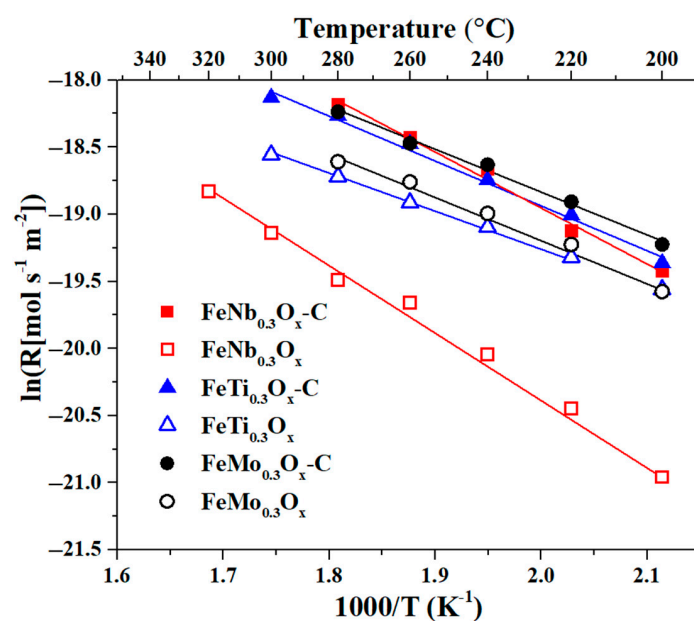


Figure 2. Arrhenius plots of the reaction rates over all the $\text{FeM}_{0.3}\text{O}_x\text{-C}$ and $\text{FeM}_{0.3}\text{O}_x$ ($M = \text{Nb, Ti, Mo}$) samples. Reaction conditions: $[\text{NO}] = [\text{NH}_3] = 500$ ppm, $[\text{O}_2] = 5$ vol %, N_2 balance, with the NO_x conversion below 25%.

Table 1. Activation energy and reaction rate at 260 °C of all the $\text{FeM}_{0.3}\text{O}_x\text{-C}$ and $\text{FeM}_{0.3}\text{O}_x$ ($M = \text{Nb, Ti, Mo}$) samples.

	E_a (kJ mol^{-1})	R^2	Reaction Rate at 260 °C ($\text{mol m}^{-2} \text{s}^{-1}$)
$\text{FeNb}_{0.3}\text{O}_x\text{-C}$	34.5	0.991	9.9×10^{-9}
$\text{FeNb}_{0.3}\text{O}_x$	40.0	0.993	2.9×10^{-9}
$\text{FeTi}_{0.3}\text{O}_x\text{-C}$	28.0	0.993	9.5×10^{-9}
$\text{FeTi}_{0.3}\text{O}_x$	22.6	0.999	6.1×10^{-9}
$\text{FeMo}_{0.3}\text{O}_x\text{-C}$	26.3	0.993	9.5×10^{-9}
$\text{FeMo}_{0.3}\text{O}_x$	26.2	0.990	7.1×10^{-9}

2.3. Structural Properties

2.3.1. N₂-Physisorption Analysis

The surface areas and pore volumes of all the samples are summarized and displayed in Table 2. The FeNb_{0.3}O_x-C catalyst showed a smaller surface area than that of FeNb_{0.3}O_x (172 m² g⁻¹ vs. 210 m² g⁻¹) while exhibiting a larger average pore size. A decrease in surface area induced by the assistance of CTAB in the preparation process was also observed for Fe-Ti and Fe-Mo, with detailed information shown in Table 2.

Table 2. Structural parameters of all the FeM_{0.3}O_x-C and FeM_{0.3}O_x (M = Nb, Ti, Mo) samples.

	Surface Area (m ² g ⁻¹)	Pore Volume (cm ³ g ⁻¹)
FeNb _{0.3} O _x -C	172	0.25
FeNb _{0.3} O _x	210	0.13
FeTi _{0.3} O _x -C	151	0.21
FeTi _{0.3} O _x	191	0.24
FeMo _{0.3} O _x -C	99	0.15
FeMo _{0.3} O _x	167	0.24

2.3.2. XRD Analysis

The XRD patterns in Figure 3 illustrate the crystalline phases of the synthesized samples. Diffraction peaks associated with γ -Fe₂O₃ appeared for the FeNb_{0.3}O_x-C catalyst, while no peak due to Nb species was observed. For the FeNb_{0.3}O_x catalyst, no characteristic peaks due to Fe or Nb components were observed, indicating their high dispersion or amorphous state [37]. For FeTi_{0.3}O_x, only peaks attributed to α -Fe₂O₃ could be observed, while for FeTi_{0.3}O_x-C, besides the peaks of α -Fe₂O₃ with lower intensity, peaks of γ -Fe₂O₃ appeared. As for the Fe-Mo catalysts, interestingly, only peaks due to γ -Fe₂O₃ were observed for the FeMo_{0.3}O_x-C catalyst, whereas all the peaks were assignable to α -Fe₂O₃ in the case of FeMo_{0.3}O_x. As γ -Fe₂O₃ and other iron oxides (such as Fe₃O₄) show very similar diffraction patterns [38], ⁵⁷Fe Mössbauer spectroscopy measurements were carried out to confirm the crystalline phase of the iron oxides present, with results shown in Figure S2. The data were fitted using Moss Winn with parameters including isomer shift (mm s⁻¹), quadrupole splitting (mm s⁻¹), internal hyperfine field (T), and area listed in Table S1. According to previous research [39–44], the isomer shift values of doublets indicated the signals from Fe³⁺ for each sample. In other words, no signal of Fe²⁺ was observed, which ruled out the possibility of Fe₃O₄ in Fe-M-C catalysts. The values of isomer shift around 0.32 mm s⁻¹ and internal hyperfine field around 49.8 T of sextets confirmed the presence of γ -Fe₂O₃ in FeNb_{0.3}O_x-C, FeTi_{0.3}O_x-C, and FeMo_{0.3}O_x-C. In addition, the values of isomer shift around 0.38 mm s⁻¹ and internal hyperfine field around 51.2 T of sextets for FeTi_{0.3}O_x-C, FeTi_{0.3}O_x, and FeMo_{0.3}O_x were ascribed to α -Fe₂O₃. These results were in good agreement with XRD results. Based on the results, the ratio of γ -Fe₂O₃ and α -Fe₂O₃ components in FeTi_{0.3}O_x-C was further calculated from the areas in Table S1 with the value of about 3:1 [44].

2.4. Acidity and Redox Ability

2.4.1. Acidic Properties

In the NH₃-SCR reaction, acid sites on the catalysts are responsible for the adsorption of ammonia and play an important role in NO_x reduction. To investigate the surface acidity, NH₃-TPD experiments were carried out, and the amount of NH₃ desorption that occurred was calculated. For all the catalysts, one peak at around 150 °C and another peak around 300 °C were observed, which correspond to weakly adsorbed and strongly adsorbed ammonia species, respectively [45]. To reduce errors in the determination of the NH₃ desorption amount, the NH₃-TPD experiments were repeated two times (Figure S3a,b), with results shown in Figure S3c and Table 3. The total amount of NH₃ desorbed from FeNb_{0.3}O_x-C was around 260 μ mol g⁻¹, less than that for FeNb_{0.3}O_x (around 289 μ mol g⁻¹). After normalization by surface area (that is, the NH₃ adsorption amount divided by the surface

area), the calculated NH_3 desorption value was $1.5 \mu\text{mol m}^{-2}$ for $\text{FeNb}_{0.3}\text{O}_x\text{-C}$, which was larger than that for $\text{FeNb}_{0.3}\text{O}_x$ ($1.4 \mu\text{mol m}^{-2}$). For Fe–Ti and Fe–Mo, $\text{FeM}_{0.3}\text{O}_x\text{-C}$ catalysts also showed lower NH_3 desorption but a higher value after normalization by surface area compared with $\text{FeM}_{0.3}\text{O}_x$ catalysts. In addition, the percentages of weakly adsorbed ammonia species were calculated and are shown in Table 3, with the values of $\text{FeM}_{0.3}\text{O}_x\text{-C}$ catalysts being slightly higher than those of the $\text{FeM}_{0.3}\text{O}_x$ catalysts, respectively.

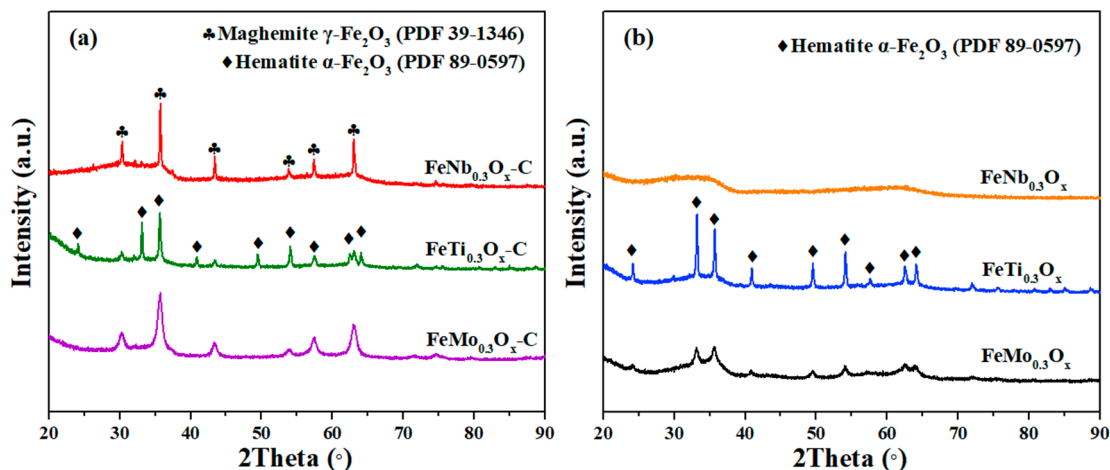


Figure 3. XRD patterns of (a) $\text{FeM}_{0.3}\text{O}_x\text{-C}$ and (b) $\text{FeM}_{0.3}\text{O}_x$ ($M = \text{Nb, Ti, Mo}$) samples.

Table 3. Desorption amount of NH_3 and percentage of weak-adsorbed NH_3 over all the $\text{FeM}_{0.3}\text{O}_x\text{-C}$ and $\text{FeM}_{0.3}\text{O}_x$ ($M = \text{Nb, Ti, Mo}$) samples.

	NH_3 Desorption Amount ($\mu\text{mol g}^{-1}$) *	NH_3 Desorption Amount Normalized by Surface Area ($\mu\text{mol m}^{-2}$)	Percentage of Weak-Adsorbed NH_3 (%)
$\text{FeNb}_{0.3}\text{O}_x\text{-C}$	260 ± 7.0	1.5 ± 0.05	75.9 ± 1.3
$\text{FeNb}_{0.3}\text{O}_x$	289 ± 7.6	1.4 ± 0.07	72.8 ± 1.1
$\text{FeTi}_{0.3}\text{O}_x\text{-C}$	226 ± 4.7	1.5 ± 0.03	75.9 ± 0.1
$\text{FeTi}_{0.3}\text{O}_x$	246 ± 12.7	1.3 ± 0.08	74.2 ± 1.2
$\text{FeMo}_{0.3}\text{O}_x\text{-C}$	145 ± 8.3	1.5 ± 0.12	79.2 ± 1.7
$\text{FeMo}_{0.3}\text{O}_x$	229 ± 15.2	1.4 ± 0.08	77.9 ± 1.2

* with experiments and error bars shown in Figure S3.

To identify the types of acid sites, DRIFT studies of NH_3 adsorption at 150°C were performed and shown in Figure 4. The bands at 1672 cm^{-1} and 1430 cm^{-1} were attributed to NH_4^+ species adsorbed on Brønsted acid sites, and bands at 1606 cm^{-1} and 1209 cm^{-1} were ascribed to NH_3 species adsorbed on Lewis acid sites [46–48]. By comparing the intensity of bands at 1430 cm^{-1} , one can easily observe that more NH_4^+ species adsorbed on Brønsted acid sites on $\text{FeM}_{0.3}\text{O}_x\text{-C}$ catalysts than on $\text{FeM}_{0.3}\text{O}_x$ catalysts. In contrast, as indicated by the intensity of the band at 1606 cm^{-1} , the amount of NH_3 species adsorbed on Lewis acid sites on $\text{FeM}_{0.3}\text{O}_x\text{-C}$ catalysts was slightly lower than that for $\text{FeM}_{0.3}\text{O}_x$ catalysts.

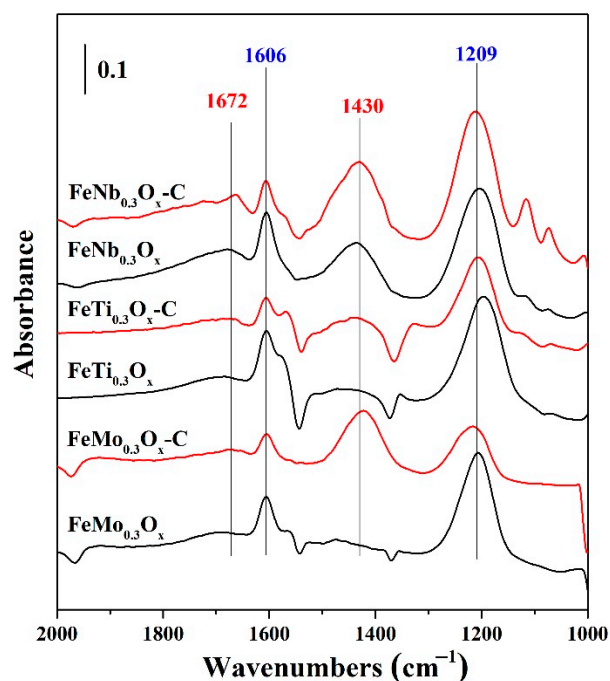


Figure 4. In situ DRIFTS of adsorption of NH_3 species over all the $\text{FeM}_{0.3}\text{O}_x\text{-C}$ and $\text{FeM}_{0.3}\text{O}_x$ ($M = \text{Nb, Ti, Mo}$) samples at 150°C . Before measurement, each sample was pretreated in 500 ppm NH_3/N_2 for 0.5 h and then purged by N_2 for 0.5 h.

2.4.2. XPS Analysis

To explore the electronic states and atomic concentrations of surface atoms, XPS analysis was carried out for all the samples. As shown in Figure 5, the O 1s spectra could be fitted into two peaks, with the peak at around 530.1 eV corresponding to lattice oxygen (denoted as O_β) and the peak at around 531.4 eV assignable to surface oxygen (denoted as O_α). Compared with $\text{FeM}_{0.3}\text{O}_x$ catalysts, the O_β species in $\text{FeM}_{0.3}\text{O}_x\text{-C}$ catalysts showed higher binding energy. Meanwhile, the ratios of $\text{O}_\alpha/(\text{O}_\alpha + \text{O}_\beta)$, as well as the proportion of O_α (that is, the value of $\text{O}_\alpha/(\text{O}_\alpha + \text{O}_\beta)$ plus the value of the O atom ratio on the surface), were calculated. As listed in Table 4, each of the $\text{FeM}_{0.3}\text{O}_x\text{-C}$ catalysts showed a higher proportion of O_α than the corresponding $\text{FeM}_{0.3}\text{O}_x$ catalysts, indicative of a higher content of surface O species on $\text{FeM}_{0.3}\text{O}_x\text{-C}$.

The XPS Spectra of Nb 3d, Ti 2p, and Mo 3d are shown in Figure S4, showing Nb, Ti, and Mo elements in their highest valence state [49–54]. In addition, it was observed that the acid components (Nb, Ti, and Mo) in the $\text{FeM}_{0.3}\text{O}_x\text{-C}$ catalysts showed higher binding energy than those in $\text{FeM}_{0.3}\text{O}_x$ catalysts. The spectra of Fe 2p are shown in Figure S5, with the peaks located around 724.5 eV, 718.9 eV and 710.7 eV, which correspond to Fe $2p_{1/2}$, Fe $2p_{3/2}$ satellite and Fe $2p_{3/2}$, respectively, corresponding to Fe^{3+} [45,46]. As shown in Table 4, for a given acid component, the ratio of M/Fe in $\text{FeM}_{0.3}\text{O}_x\text{-C}$ catalysts was always higher than that in $\text{FeM}_{0.3}\text{O}_x$ catalysts. This result indicated that a surface enrichment of acid components was induced by CTAB addition during the process of catalyst preparation, which was consistent with the results of $\text{NH}_3\text{-TPD}$.

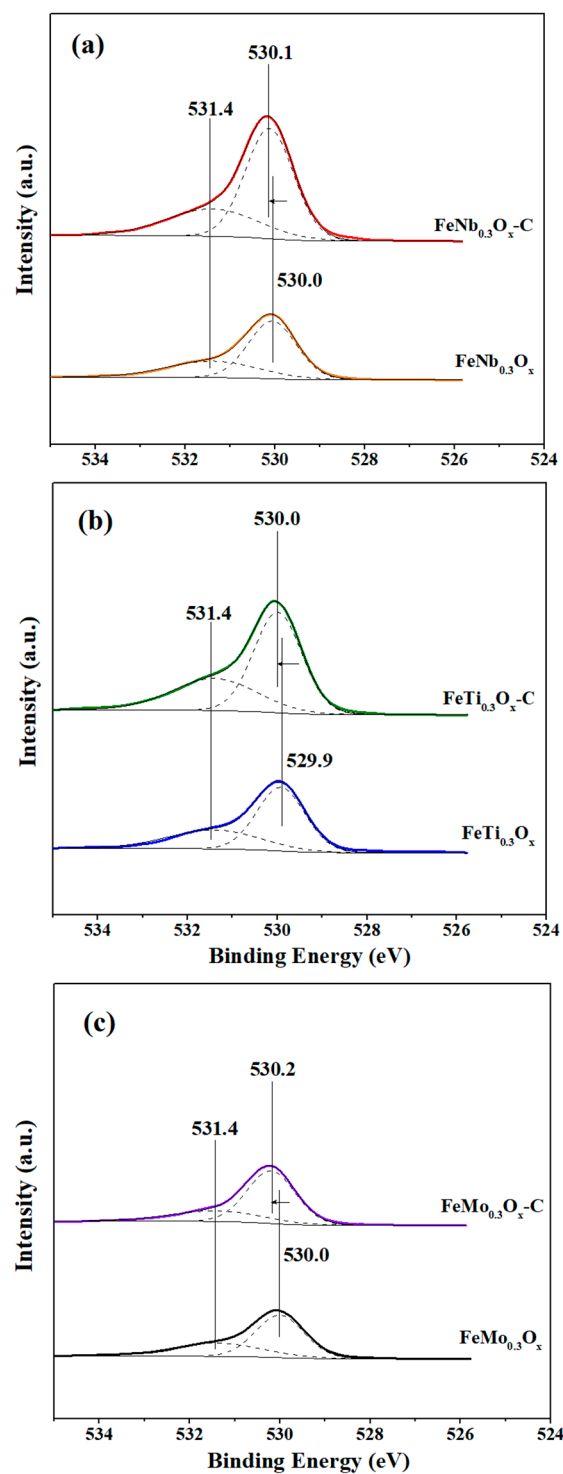


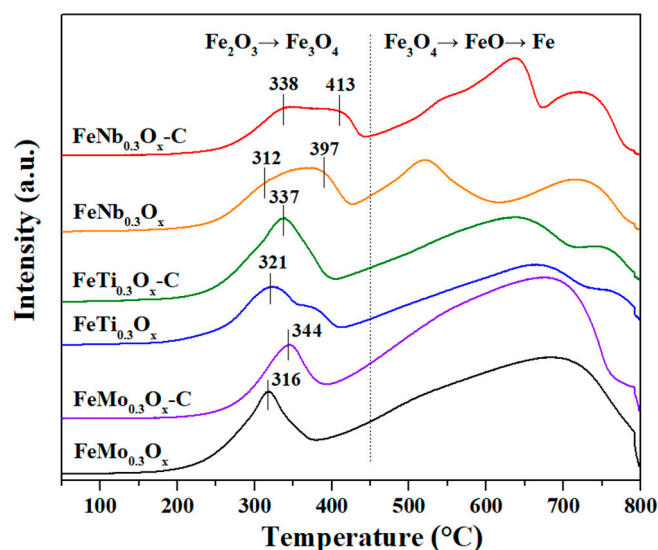
Figure 5. XPS spectra of O 1s over (a) FeNb_{0.3}O_x-C and FeNb_{0.3}O_x; (b) FeTi_{0.3}O_x-C and FeTi_{0.3}O_x; (c) FeMo_{0.3}O_x-C and FeMo_{0.3}O_x.

Table 4. Surface components of all the $\text{FeM}_{0.3}\text{O}_x\text{-C}$ and $\text{FeM}_{0.3}\text{O}_x$ ($M = \text{Nb, Ti, Mo}$) samples from XPS results.

	Proportion of O	$\text{O}_\alpha/(\text{O}_\alpha + \text{O}_\beta)$	Proportion of O_α	M/Fe
$\text{FeNb}_{0.3}\text{O}_x\text{-C}$	49.4%	33.2%	16.4%	0.49
$\text{FeNb}_{0.3}\text{O}_x$	48.5%	32.6%	15.8%	0.43
$\text{FeTi}_{0.3}\text{O}_x\text{-C}$	50.7%	38.7%	19.6%	0.72
$\text{FeTi}_{0.3}\text{O}_x$	48.3%	36.4%	17.6%	0.45
$\text{FeMo}_{0.3}\text{O}_x\text{-C}$	52.5%	33.3%	17.5%	0.97
$\text{FeMo}_{0.3}\text{O}_x$	49.6%	35.0%	17.4%	0.55

2.4.3. H_2 -TPR Analysis

To further investigate the reducibility of the prepared catalysts, H_2 -TPR experiments were carried out. As shown in Figure 6, the peaks below 450 °C correspond to the reduction of Fe_2O_3 to Fe_3O_4 . Further reduction of Fe_3O_4 to FeO and Fe occurred at higher temperatures (above 450 °C) [13,55,56]. Over the $\text{FeNb}_{0.3}\text{O}_x\text{-C}$ catalyst, it was observed that the peaks due to the reduction of Fe_2O_3 to Fe_3O_4 were centered at higher temperatures (348 °C and 413 °C) compared with $\text{FeNb}_{0.3}\text{O}_x$ (centered at 312 °C and 397 °C). Such weakening of the redox ability of Fe by CTAB addition was also observed during the reduction of Fe_3O_4 to FeO and Fe . As for $\text{FeTi}_{0.3}\text{O}_x\text{-C}$ and $\text{FeMo}_{0.3}\text{O}_x\text{-C}$, similarly, the reduction peaks of Fe_2O_3 occurred more clearly at higher temperatures compared with those of $\text{FeTi}_{0.3}\text{O}_x$ and $\text{FeMo}_{0.3}\text{O}_x$, respectively.

**Figure 6.** H_2 -TPR results of all the $\text{FeM}_{0.3}\text{O}_x\text{-C}$ and $\text{FeM}_{0.3}\text{O}_x$ ($M = \text{Nb, Ti, Mo}$) samples in a flow of 10 vol % H_2/N_2 with the heating rate of 10 °C min^{-1} . Before measurement, the sample was pretreated in N_2 at 300 °C for 1 h, and purged by N_2 for 0.5 h.

2.4.4. Direct Oxidation of NH_3 and NO

Direct oxidation reactions of NH_3 and NO were also conducted, with results shown in Figures S6 and S7, respectively. At temperatures below 250 °C, the direct oxidation of NH_3 hardly occurred over any of the samples, benefiting the NH_3 -SCR reaction. At temperatures above 250 °C, NH_3 conversion increased with rising temperature, during which the $\text{FeM}_{0.3}\text{O}_x\text{-C}$ always exhibited lower activity for NH_3 oxidation than $\text{FeM}_{0.3}\text{O}_x$ (except for $\text{FeNb}_{0.3}\text{O}_x\text{-C}$ at the temperature of 400 °C). This was possibly due to the weakened redox ability induced by CTAB addition. By contrast, the direct oxidation of NO occurred over the whole temperature range, during which the NO conversion increased with rising temperature, reached a maximum value, and then decreased. Interestingly, $\text{FeM}_{0.3}\text{O}_x\text{-C}$ always showed higher activity for NO_2 formation (except for $\text{FeMo}_{0.3}\text{O}_x\text{-C}$ at

temperatures above 250 °C). These results suggested that the intrinsic properties governing the direct oxidation of NO were different from that of NH₃ oxidation. Combined with the results listed in Table 4, it can be deduced that surface oxygen plays a crucial role in NO oxidation to NO₂ over the Fe–M catalysts [6,57,58].

3. Discussion

The SCR performance results (Figure 1 and Figure S1) and kinetic studies (Figure 2) showed that FeM_{0.3}O_x-C catalysts showed higher SCR activity as well as N₂ selectivity than FeM_{0.3}O_x catalysts over the whole temperature range. It can be concluded from XRD (Figure 3) and Mössbauer spectra (Figure S2 and Table S1) that the addition of CTAB into solutions of precursors promoted the formation of γ -Fe₂O₃, which was more active in terms of SCR activity than α -Fe₂O₃ (Figure S8). Specifically, combining the XRD results with the kinetic studies, it was clear that samples containing the γ -Fe₂O₃ phase (FeM_{0.3}O_x-C catalysts) showed similar intrinsic activity. Meanwhile, FeTi_{0.3}O_x and FeMo_{0.3}O_x catalysts with pure α -Fe₂O₃ phase exhibited almost the same reaction rate, which was lower than that of the FeM_{0.3}O_x-C catalysts. This illustrated that the formation of the γ -Fe₂O₃ phase induced by CTAB addition during the catalyst preparation process improved the catalytic activity of FeM_{0.3}O_x. As shown in Figure 3, meanwhile, the Fe phase in FeNb_{0.3}O_x-C and FeMo_{0.3}O_x-C detected by XRD was 100% γ -Fe₂O₃, while both the γ -Fe₂O₃ and α -Fe₂O₃ phases were observed in FeTi_{0.3}O_x-C. Taking these findings into account, it would be expected that the FeNb_{0.3}O_x-C and FeMo_{0.3}O_x-C would be more active for NH₃-SCR than FeTi_{0.3}O_x-C. By comparing the results of Figure 1 with those of Figure S8, it can be easily found that, at a given temperature, the activity of the pure γ -Fe₂O₃ sample was much lower than FeNb_{0.3}O_x-C and FeTi_{0.3}O_x-C. These results, in turn, indicate that other factors also have a great influence on the catalytic performance of the Fe–M system.

It is well-accepted that optimizing the acid-redox properties is crucial to designing SCR catalysts with high catalytic performance. In our research, the alteration of the crystalline phase modified both the acidity and reducibility of the Fe–M catalysts, which played a significant role in the improved SCR performance. As for acidity, despite the smaller surface area (Table 2) and lower total desorption amount of NH₃ (Table 3), FeM_{0.3}O_x-C catalysts showed higher exposure of acid sites. This was explained by the increased ratio of M/Fe on FeM_{0.3}O_x-C catalysts revealed by XPS (Table 4), consistent with higher exposure of acid components. The NH₃-TPD results (Figure 4) indicated more weakly adsorbed ammonia on FeM_{0.3}O_x-C catalysts. As previous research indicated the weaker stability of NH₄⁺ species adsorbed on Brønsted acid sites compared to NH₃ species adsorbed on Lewis acid sites [59,60], this suggested that more NH₄⁺ species adsorbed on Brønsted acid sites existed on FeM_{0.3}O_x-C catalysts. This was further confirmed by the DRIFT results (Figure 5). In conclusion, increased exposure of acid components, especially Brønsted acid sites, was observed over FeM_{0.3}O_x-C catalysts, which benefited SCR activity [45,61,62].

For metal oxide NH₃-SCR catalysts, generally, surface oxygen (O_α) is important for the oxidation of NO to NO₂, thus promoting the “fast-SCR” reaction at low-temperature [6,57,58]. In addition, the over-oxidation of NH₃ accounted for the decreased NO_x conversion at high temperatures [1,13,16,63,64]. In our research, on one hand, the increased percentage of surface O_α boosted the oxidation of NO to NO₂ (as shown in Table 4 and Figure S7), thus benefiting the activity at low temperatures. On the other hand, the weaker reducibility of Fe species revealed by H₂-TPR (Figure 6) suppressed the over-oxidation of NH₃ over FeTi_{0.3}O_x-C and FeMo_{0.3}O_x-C catalysts at high temperatures (Figure S6), explaining the improved NO_x conversion and N₂ selectivity. As a result, the SCR performance of FeM_{0.3}O_x-C catalysts over the whole temperature range was improved. In addition, the shift of binding energy for O 1s, Nb 3d, Ti 2p, and Mo 3d in XPS results associated with the addition of CTAB was possibly due to deviation of the electron cloud [65–67], which indicated enhanced interaction between Fe and acid components and was related to the observed change in the crystalline phase.

Compared with FeNb_{0.3}O_x-C, FeTi_{0.3}O_x-C exhibited a higher proportion of surface oxygen (Table 4) and a higher ability for NO oxidation to NO₂ (Figure S7). As discussed above, the surface oxygen species were active for the oxidation of NO to NO₂, thus promoting the “fast-SCR” reaction at low-temperature. With this in mind, it is reasonable that FeTi_{0.3}O_x-C shows similar intrinsic activity to FeNb_{0.3}O_x-C, even though the latter exhibits a 100% γ-Fe₂O₃ phase. As shown in Table 3, the desorption amount of NH₃ over FeMo_{0.3}O_x-C was slightly lower than that of FeTi_{0.3}O_x-C, suggesting that a smaller amount of acid sites was available for NH₃-SCR. Compared with FeTi_{0.3}O_x-C, FeMo_{0.3}O_x-C also exhibited a lower proportion of surface oxygen (Table 4), resulting in lower activity for NO oxidation to NO₂ (Figure S7), which is not beneficial for the occurrence of fast-SCR. Taking these facts into account, it is reasonable that FeMo_{0.3}O_x-C shows similar intrinsic activity to FeTi_{0.3}O_x-C, even though the former contains 100% γ-Fe₂O₃.

4. Materials and Methods

4.1. Catalyst Preparation

The CTAB-assisted co-precipitation process was inspired by previous research on FeMnTi catalysts by Wu et al. [68]. Typically, CTAB was first dissolved into deionized water, and then precursors containing Fe(NO₃)₃·9H₂O, C₁₀H₅NbO₂₀ (or Ti(SO₄)₂, and (NH₄)₆Mo₇O₂₄·4H₂O) in the required molar ratios were added to the CTAB solution. The molar ratio of M:Fe (M = Nb, Ti and Mo) was set at 3:10. After stirring for 1 h, the solution was heated to 90 °C and kept for 10 h. The obtained precipitates were filtered, washed and dried overnight at 105 °C. Then the samples were calcined at 400 °C for 5 h. The obtained catalysts were labeled as FeM_{0.3}O_x-C (i.e., FeNb_{0.3}O_x-C, FeTi_{0.3}O_x-C, and FeMo_{0.3}O_x-C, respectively). For comparative purposes, catalysts without CTAB were also prepared in the same way and labeled as FeM_{0.3}O_x (FeNb_{0.3}O_x, FeTi_{0.3}O_x, and FeMo_{0.3}O_x). Commercial pure γ-Fe₂O₃ and pure α-Fe₂O₃ were also used for comparison. Before NH₃-SCR activity tests, all the samples were pressed, crushed, and sieved to 40–60 mesh.

4.2. Activity Test

The NH₃-SCR activities were tested in a fixed-bed quartz tube flow reactor with an inner diameter of 4 mm (at GHSV of 500,000 h⁻¹, the mass of each catalyst was around 60 mg). The feed gas consisted of 500 ppm of NO, 500 ppm of NH₃, 5 vol % O₂, balanced by N₂, with a gas flow rate of 500 mL min⁻¹. The concentrations of NH₃, NO, NO₂, and N₂O were continually monitored by FTIR spectrometer (IS10 Nicolet) (City, State, Abbr(if has), Country)(Thermo, Waltham, MA USA), which was equipped with a multiple path gas cell (2 m).

The NO_x conversion and N₂ selectivity were calculated as follows [69,70]:

$$\text{NO}_x \text{ conversion}(\%) = \left(1 - \frac{[\text{NO}_x]_{\text{out}}}{[\text{NO}_x]_{\text{in}}} \right) \times 100\% \quad (1)$$

$$\text{N}_2 \text{ selectivity}(\%) = \left(1 - \frac{2[\text{N}_2\text{O}]_{\text{out}}}{[\text{NO}_x]_{\text{in}} - [\text{NO}_x]_{\text{out}} + [\text{NH}_3]_{\text{in}} - [\text{NH}_3]_{\text{out}}} \right) \times 100\% \quad (2)$$

with [NO_x] = [NO] + [NO₂].

4.3. Kinetic Study

The apparent activation energy (E_a) and reaction order for NO_x reduction were measured in a fixed-bed quartz tube flow reactor with an inner diameter of 4 mm. In this case, the mass of each catalyst was 20 mg, and the conversion of NO_x was controlled below 25%. The feed gas composition was 500 ppm NO, 500 ppm NH₃, 5% O₂, and N₂ balance. The reaction rate of NO_x conversion was calculated as follows:

$$-R_{\text{NO}_x} = \frac{F_{\text{NO}_x} \times X_{\text{NO}_x}}{W \times S} \quad (3)$$

where F_{NO_x} is the molar flow rate of NO_x , X_{NO_x} is the conversion of NO_x , W is the weight of the catalyst, and S is the BET (Brunauer–Emmett–Teller) surface area.

4.4. Catalyst Characterization

N_2 -physisorption analysis was obtained at 77 K using a Quantachrome Autosorb-1C instrument (Anton Paar, Graz, Austria) at liquid nitrogen temperature. The specific surface areas were calculated by the BET equation in the 0.05–0.30 partial pressure range. The pore volumes and average pore diameters were determined by the BJH method from the desorption branches of the isotherms. Prior to each N_2 -physisorption analysis, the samples were degassed at 300 °C for 3 h. Powder X-ray diffraction (XRD) patterns of the samples were conducted on a Bruker D8 diffractometer (Bruker, Karlsruhe, Germany) with $\text{Cu K}\alpha$ ($\lambda = 0.15406$ nm) radiation. The scan range of 2θ range was from 20° to 90° with a step size of 0.02°.

The temperature-programmed desorption of ammonia (NH_3 -TPD) experiments were carried out on a fixed-bed quartz tube flow reactor with an inner diameter of 4 mm. The concentration of NH_3 was continually monitored by an FTIR spectrometer (IS10 Nicolet), which was equipped with a multiple path gas cell (2 m). Prior to each TPD experiment, the 100 mg samples were pretreated in 20% O_2/N_2 at a flow rate of 300 mL min^{-1} at 350 °C for 0.5 h, and then cooled down to 50 °C and purged by N_2 for 0.5 h. The samples were then exposed to a flow of 500 ppm NH_3/N_2 (500 mL min^{-1}) at 50 °C for 0.5 h, followed by N_2 purging for 0.5 h. Finally, the temperature was raised to 800 °C in N_2 with the rate of 10 °C min^{-1} . In situ DRIFTS experiments were performed on an FTIR spectrometer (Nicolet IS50) equipped with an MCT/A detector cooled by liquid nitrogen. Each catalyst was pretreated in 20 vol % O_2/N_2 at 400 °C for 0.5 h and then cooled down to 150 °C. The samples were exposed to a flow of 500 ppm NH_3 with an N_2 balance for 0.5 h and purged by N_2 for another 0.5 h. XPS measurements were carried out on an X-ray photoelectron spectrometer (Thermo Fisher Scientific K-Alpha, Thermo, Waltham, MA, USA) with Al $\text{K}\alpha$ radiation (1486.8 eV) at an energy resolution of 0.05 eV (Ag 3d_{5/2}). The binding energies of Fe 2p, Nb 3d, Ti 2p, Mo 3d, and O 1s were calibrated using the C 1s peak (BE = 284.8 eV) as standard. The temperature-programmed reduction of hydrogen (H_2 -TPR) experiments were carried out on a Auto Chem 2920 chemisorption analyzer (Micromeritics, Aachen, Germany). In a typical measurement, 150 mg of the sample was first, preprocessed in a flow of N_2 with the total flow rate of 50 mL min^{-1} at 300 °C for 1 h, and then cooled to 50 °C, followed by N_2 purging for another 0.5 h. Then the temperature was linearly increased from 50 to 900 °C at the heating rate of 10 °C min^{-1} in a flow of 10 vol % H_2/N_2 (50 mL min^{-1}), during which the H_2 consumption was continuously recorded by a thermal conductivity detector (TCD).

5. Conclusions

In our research, $\text{FeM}_{0.3}\text{O}_x\text{-C}$ catalysts synthesized with the assistance of CTAB exhibited higher SCR performance compared with $\text{FeM}_{0.3}\text{O}_x$. Characterization revealed that the presence of CTAB in the preparation process of Fe–M (M= Nb, Ti, Mo) composite oxides adjusted the crystalline phase of iron oxides and modified both the reducibility and acidity. The optimized catalysts exposed more surface acid sites, which was beneficial to the SCR activity. In addition, surface oxygen was increased, which benefited the NO oxidation and the “fast SCR” reaction. In addition, the redox ability of Fe was weakened by the addition of CTAB, thus restraining the over-oxidation of NH_3 and improved NO_x conversion as well as N_2 selectivity at high temperatures. Overall, both the acidity and reducibility were tuned by CTAB addition during the process of catalyst preparation; thus, $\text{FeM}_{0.3}\text{O}_x\text{-C}$ catalysts achieved higher catalytic performance over the whole temperature range.

Supplementary Materials: The following are available online at <https://www.mdpi.com/2073-4344/11/2/224/s1>, Figure S1: N_2 selectivity over all the samples. Reaction conditions: $[\text{NO}] = [\text{NH}_3] = 500$ ppm, $[\text{O}_2] = 5$ vol %, N_2 balance, GHSV = 500,000 h^{-1} , Figure S2: Mössbauer spectra of all the samples at room temperature, Figure S3. (a) NH_3 -TPD results of all the $\text{FeM}_{0.3}\text{O}_x\text{-C}$ and $\text{FeM}_{0.3}\text{O}_x$ (M = Nb, Ti, Mo) samples in a flow of N_2 with a heating rate of 10 °C min^{-1} . Before measurement,

each sample was pretreated in 20% O₂/N₂ at 350 °C for 0.5 h, then exposed to 500 ppm NH₃/N₂ at 50 °C for 0.5 h, and purged by N₂ for 0.5 h. (b) Repeated NH₃-TPD results and (c) NH₃ desorption amount of all the FeM_{0.3}O_x-C and FeM_{0.3}O_x (M = Nb, Ti, Mo) samples with error bars, Figure S4: XPS spectra of (a) Nb 3d; (b) Ti 2p; and (c) Mo 3d over FeM_{0.3}O_x-C and FeM_{0.3}O_x (M = Nb, Ti, Mo) samples, Figure S5: XPS spectra of Fe 2p over FeM_{0.3}O_x-C and FeM_{0.3}O_x (M = Nb, Ti, Mo) samples, Figure S6: Direct oxidation of NH₃ over all the samples. Reaction conditions: [NH₃] = 500 ppm, [O₂] = 5 vol %, N₂ balance, GHSV = 250,000 h⁻¹, Figure S7: Direct oxidation of NO over all the samples. Reaction conditions: [NO] = 500 ppm, [O₂] = 5 vol %, N₂ balance, GHSV = 250,000 h⁻¹, Figure S8: NO_x conversion over pure γ-Fe₂O₃ and pure α-Fe₂O₃. Reaction conditions: [NO] = [NH₃] = 500 ppm, [O₂] = 5 vol %, N₂ balance, GHSV = 500,000 h⁻¹, Table S1: Isomer shift (mm s⁻¹), quadrupole splitting (mm s⁻¹), internal hyperfine field (T), and area of sub-spectra from Mössbauer.

Author Contributions: Conceptualization, W.Z., Y.Y. and H.H.; methodology, X.S. and J.L.; investigation, W.Z., Z.L. and Y.H.; data curation, W.Z., M.G. and C.C.; writing—original draft preparation, W.Z. and Y.W.; writing—review and editing, X.S. and Y.Y. All authors have read and agreed to the published version of the manuscript.

Funding: This research was funded by the National Natural Science Foundation of China (grant number 21673277 and 21637005) and the Strategic Priority Research Program of the Chinese Academy of Sciences (grant number XDA23010200).

Data Availability Statement: The data presented in this study are available on request from the corresponding author.

Conflicts of Interest: The authors declare no conflict of interest.

References

1. Han, L.; Cai, S.; Gao, M.; Hasegawa, J.Y.; Wang, P.; Zhang, J.; Shi, L.; Zhang, D. Selective catalytic reduction of NO_x with NH₃ by using novel catalysts: State of the art and future prospects. *Chem. Rev.* **2019**, *119*, 10916–10976. [[CrossRef](#)]
2. Shan, W.; Yu, Y.; Zhang, Y.; He, G.; Peng, Y.; Li, J.; He, H. Theory and practice of metal oxide catalyst design for the selective catalytic reduction of NO with NH₃. *Catal. Today* **2020**. [[CrossRef](#)]
3. Granger, P.; Parvulescu, V.I. Catalytic NO_x abatement systems for mobile sources: From three-way to lean burn after-treatment technologies. *Chem. Rev.* **2011**, *111*, 3155–3207. [[CrossRef](#)]
4. Liu, F.; Yu, Y.; He, H. Environmentally-benign catalysts for the selective catalytic reduction of NO_x from diesel engines: Structure-activity relationship and reaction mechanism aspects. *Chem. Commun.* **2014**, *50*, 8445–8463. [[CrossRef](#)] [[PubMed](#)]
5. Marberger, A.; Ferri, D.; Elsener, M.; Krocher, O. The significance of Lewis acid sites for the selective catalytic reduction of nitric oxide on vanadium-based catalysts. *Angew. Chem. Int. Ed. Engl.* **2016**, *55*, 11989–11994. [[CrossRef](#)]
6. Liu, F.; He, H.; Zhang, C.; Feng, Z.; Zheng, L.; Xie, Y.; Hu, T. Selective catalytic reduction of NO with NH₃ over iron titanate catalyst: Catalytic performance and characterization. *Appl. Catal. B Environ.* **2010**, *96*, 408–420. [[CrossRef](#)]
7. Yang, S.; Li, J.; Wang, C.; Chen, J.; Ma, L.; Chang, H.; Chen, L.; Peng, Y.; Yan, N. Fe–Ti spinel for the selective catalytic reduction of NO with NH₃: Mechanism and structure–activity relationship. *Appl. Catal. B Environ.* **2012**, *117–118*, 73–80. [[CrossRef](#)]
8. Liu, J.; Meeprasert, J.; Namuangruk, S.; Zha, K.; Li, H.; Huang, L.; Maitarad, P.; Shi, L.; Zhang, D. Facet–activity relationship of TiO₂ in Fe₂O₃/TiO₂ nanocatalysts for selective catalytic reduction of NO with NH₃: In situ DRIFTS and DFT studies. *J. Phys. Chem. C* **2017**, *121*, 4970–4979. [[CrossRef](#)]
9. Xin, Y.; Zhang, N.; Li, Q.; Zhang, Z.; Cao, X.; Zheng, L.; Zeng, Y.; Anderson, J.A. Active site identification and modification of electronic states by atomic-scale doping to enhance oxide catalyst innovation. *ACS Catal.* **2018**, *8*, 1399–1404. [[CrossRef](#)]
10. Chen, Y.; Li, C.; Chen, J.; Tang, X. Self-prevention of well-defined-facet Fe₂O₃/MoO₃ against deposition of ammonium bisulfate in low-temperature NH₃-SCR. *Environ. Sci. Technol.* **2018**, *52*, 11796–11802. [[CrossRef](#)]
11. Qu, W.; Liu, X.; Chen, J.; Dong, Y.; Tang, X.; Chen, Y. Single-atom catalysts reveal the dinuclear characteristic of active sites in NO selective reduction with NH₃. *Nat Commun.* **2020**, *11*, 1532. [[CrossRef](#)]
12. Wang, H.; Qu, Z.; Dong, S.; Xie, H.; Tang, C. Superior performance of Fe_{1-x}W_xO₈ for the selective catalytic reduction of NO_x with NH₃: Interaction between Fe and W. *Environ. Sci. Technol.* **2016**, *50*, 13511–13519. [[CrossRef](#)]
13. Liu, F.; Shan, W.; Lian, Z.; Liu, J.; He, H. The smart surface modification of Fe₂O₃ by WO_x for significantly promoting the selective catalytic reduction of NO_x with NH₃. *Appl. Catal. B Environ.* **2018**, *230*, 165–176. [[CrossRef](#)]
14. Xin, Y.; Zhang, N.; Li, Q.; Zhang, Z.; Cao, X.; Zheng, L.; Zeng, Y.; Anderson, J.A. Selective catalytic reduction of NO with NH₃ over short-range ordered W–O–Fe structures with high thermal stability. *Appl. Catal. B Environ.* **2018**, *229*, 81–87. [[CrossRef](#)]
15. Zhang, N.; Xin, Y.; Wang, X.; Shao, M.; Li, Q.; Ma, X.; Qi, Y.; Zheng, L.; Zhang, Z. Iron-niobium composite oxides for selective catalytic reduction of NO with NH₃. *Catal. Commun.* **2017**, *97*, 111–115. [[CrossRef](#)]
16. Liu, F.; He, H.; Zhang, C. Novel iron titanate catalyst for the selective catalytic reduction of NO with NH₃ in the medium temperature range. *Chem. Commun.* **2008**, *17*, 2043–2045. [[CrossRef](#)] [[PubMed](#)]

17. Mou, X.; Zhang, B.; Li, Y.; Yao, L.; Wei, X.; Su, D.S.; Shen, W. Rod-shaped Fe₂O₃ as an efficient catalyst for the selective reduction of nitrogen oxide by ammonia. *Angew. Chem. Int. Ed. Engl.* **2012**, *51*, 2989–2993. [[CrossRef](#)] [[PubMed](#)]
18. Qu, W.; Chen, Y.; Huang, Z.; Gao, J.; Zhou, M.; Chen, J.; Li, C.; Ma, Z.; Chen, J.; Tang, X. Active tetrahedral iron sites of γ -Fe₂O₃ catalyzing NO reduction by NH₃. *Environ. Sci. Technol. Lett.* **2017**, *4*, 246–250. [[CrossRef](#)]
19. Ning, W.; Wang, T.; Chen, H.; Yang, X.; Jin, Y. The effect of Fe₂O₃ crystal phases on CO₂ hydrogenation. *PLoS ONE* **2017**, *12*, e0182955. [[CrossRef](#)]
20. Apte, S.K.; Naik, S.D.; Sonawane, R.S.; Kale, B.B.; Baeg, J.O. Synthesis of nanosize-necked structure α - and γ -Fe₂O₃ and its photocatalytic activity. *J. Am. Ceram. Soc.* **2007**, *90*, 412–414. [[CrossRef](#)]
21. Shi, X.; Chu, B.; Wang, F.; Wei, X.; Teng, L.; Fan, M.; Li, B.; Dong, L.; Dong, L. Mn-modified CuO, CuFe₂O₄ and gamma-Fe₂O₃ three-phase strong synergistic coexistence catalyst system for NO reduction by CO with wider active window. *ACS Appl. Mater. Interfaces* **2018**, *10*, 40509–40522. [[CrossRef](#)] [[PubMed](#)]
22. Lai, J.; Shafi, K.V.P.M.; Loos, K.; Ulman, A.; Lee, Y.; Vogt, T.; Estournès, C. Doping γ -Fe₂O₃ nanoparticles with Mn(III) suppresses the transition to the α -Fe₂O₃ structure. *J. Am. Chem. Soc.* **2003**, *125*, 11470–11471. [[CrossRef](#)]
23. Machala, L.; Tucek, J.; Zboril, R. Polymorphous transformations of nanometric Iron(III) Oxide: A review. *Chem. Mater.* **2011**, *23*, 3255–3272. [[CrossRef](#)]
24. Geng, Y.; Xiong, S.; Li, B.; Peng, Y.; Yang, S. The promotion of H₃PW₁₂O₄₀ grafting on NO_x abatement over γ -Fe₂O₃: Performance and reaction mechanism. *Ind. Eng. Chem. Res.* **2018**, *57*, 13661–13670. [[CrossRef](#)]
25. Chernyshova, I.V.; Hochella, M.F., Jr.; Madden, A.S. Size-dependent structural transformations of hematite nanoparticles. 1. Phase transition. *Phys. Chem. Chem. Phys.* **2007**, *9*, 1736–1750. [[CrossRef](#)]
26. Yang, S.; He, H.; Wu, D.; Chen, D.; Liang, X.; Qin, Z.; Fan, M.; Zhu, J.; Yuan, P. Decolorization of methylene blue by heterogeneous Fenton reaction using Fe_{3-x}Ti_xO₄ (0 ≤ x ≤ 0.78) at neutral pH values. *Appl. Catal. B Environ.* **2009**, *89*, 527–535. [[CrossRef](#)]
27. Lee, J.; Kwak, S.Y. Mn-doped maghemite (gamma-Fe₂O₃) from metal-organic framework accompanying redox reaction in a bimetallic system: The structural phase transitions and catalytic activity toward NO_x removal. *ACS Omega* **2018**, *3*, 2634–2640. [[CrossRef](#)] [[PubMed](#)]
28. Li, C.; Xiong, Z.; Du, Y.; Ning, X.; Li, Z.; He, J.; Qu, X.; Lu, W.; Wu, S.; Tan, L. Promotional effect of tungsten modification on magnetic iron oxide catalyst for selective catalytic reduction of NO with NH₃. *J. Energy Inst.* **2020**. [[CrossRef](#)]
29. Bharathi, S.; Nataraj, D.; Seetha, M.; Mangalaraj, D.; Ponpandian, N.; Masuda, Y.; Senthil, K.; Yong, K. Controlled growth of single-crystalline, nanostructured dendrites and snowflakes of α -Fe₂O₃: Influence of the surfactant on the morphology and investigation of morphology dependent magnetic properties. *CrystEngComm* **2010**, *12*, 373–382. [[CrossRef](#)]
30. Sun, X.; Chen, X.; Deng, Z.; Li, Y. A CTAB-assisted hydrothermal orientation growth of ZnO nanorods. *Mater. Chem. Phys.* **2002**, *78*, 99–104. [[CrossRef](#)]
31. Wu, S.; Yao, X.; Zhang, L.; Cao, Y.; Zou, W.; Li, L.; Ma, K.; Tang, C.; Gao, F.; Dong, L. Improved low temperature NH₃-SCR performance of FeMnTiO_x mixed oxide with CTAB-assisted synthesis. *Chem. Commun.* **2015**, *51*, 3470–3473. [[CrossRef](#)]
32. Li, Y.; Han, X.; Hou, Y.; Guo, Y.; Liu, Y.; Cui, Y.; Huang, Z. In situ preparation of mesoporous iron titanium catalysts by a CTAB-assisted process for NO reduction with NH₃. *Appl. Catal. A Gen.* **2018**, *559*, 146–152. [[CrossRef](#)]
33. Ding, S.; Liu, F.; Shi, X.; He, H. Promotional effect of Nb additive on the activity and hydrothermal stability for the selective catalytic reduction of NO with NH₃ over CeZrO catalyst. *Appl. Catal. B Environ.* **2016**, *180*, 766–774. [[CrossRef](#)]
34. Lian, Z.; Liu, F.; He, H.; Shi, X.; Mo, J.; Wu, Z. Manganese–niobium mixed oxide catalyst for the selective catalytic reduction of NO_x with NH₃ at low temperatures. *Chem. Eng. J.* **2014**, *250*, 390–398. [[CrossRef](#)]
35. Fudong, L.; Hong, H. Structure-activity relationship of iron titanate catalysts in the selective catalytic reduction of NO_x with NH₃. *J. Phys. Chem. C* **2010**, *114*, 16929–16936. [[CrossRef](#)]
36. Xu, W.; Yu, Y.; Zhang, C.; He, H. Selective catalytic reduction of NO by NH₃ over a Ce/TiO₂ catalyst. *Catal. Commun.* **2008**, *9*, 1453–1457. [[CrossRef](#)]
37. Xu, H.; Liu, J.; Zhang, Z.; Liu, S.; Lin, Q.; Wang, Y.; Dai, S.; Chen, Y. Design and synthesis of highly-dispersed WO₃ catalyst with highly effective NH₃-SCR activity for NO_x abatement. *ACS Catal.* **2019**, 11557–11562. [[CrossRef](#)]
38. Yamada, Y.; Nishida, N. Iron-based nanoparticles and their Mössbauer spectra. *Radioisotopes* **2019**, *68*, 125–143. [[CrossRef](#)]
39. Liu, T.; Guo, L.; Tao, Y.; Wang, Y.B.; Wang, W.D. Synthesis and interfacial structure of nanoparticles γ -Fe₂O₃ coated with surfactant DBS and CTAB. *Nanostruct. Mater.* **1999**, *11*, 487–492. [[CrossRef](#)]
40. Guo, L.; Wu, Z.; Liu, T.; Yang, S. The effect of surface modification on the microstructure and properties of γ -Fe₂O₃ nanoparticles. *Physica E* **2000**, *8*, 199–203. [[CrossRef](#)]
41. Zhang, X.; Niu, Y.; Meng, X.; Li, Y.; Zhao, J. Structural evolution and characteristics of the phase transformations between α -Fe₂O₃, Fe₃O₄ and γ -Fe₂O₃ nanoparticles under reducing and oxidizing atmospheres. *CrystEngComm* **2013**, *15*, 8166–8172. [[CrossRef](#)]
42. Ramos Guivar, J.A.; Sanches, E.A.; Bruns, F.; Sadrollahi, E.; Morales, M.A.; López, E.O.; Litterst, F.J. Vacancy ordered γ -Fe₂O₃ nanoparticles functionalized with nanohydroxyapatite: XRD, FTIR, TEM, XPS and Mössbauer studies. *Appl. Surf. Sci.* **2016**, *389*, 721–734. [[CrossRef](#)]
43. Özdemir, Ö.; Dunlop, D.J.; Berquó, T.S. Morin transition in hematite: Size dependence and thermal hysteresis. *Geochem. Geophys. Geosyst.* **2008**, *9*, 1–12. [[CrossRef](#)]
44. Cheng, C.; Lin, C.; Chiang, R.; Lin, C.; Lyubutin, I.; Alkaev, E.; Lai, H. Synthesis of monodisperse magnetic iron oxide nanoparticles from submicrometer hematite powders. *Cryst. Growth Des.* **2008**, *8*, 877–883. [[CrossRef](#)]

45. Yu, Y.; Tan, W.; An, D.; Wang, X.; Liu, A.; Zou, W.; Tang, C.; Ge, C.; Tong, Q.; Sun, J.; et al. Insight into the SO₂ resistance mechanism on γ -Fe₂O₃ catalyst in NH₃-SCR reaction: A collaborated experimental and DFT study. *Appl. Catal. B Environ.* **2021**, *281*. [[CrossRef](#)]
46. Zhang, J.; Huang, Z.; Du, Y.; Wu, X.; Shen, H.; Jing, G. Atomic-scale insights into the nature of active sites in Fe₂O₃-supported submonolayer WO₃ catalysts for selective catalytic reduction of NO with NH₃. *Chem. Eng. J.* **2020**, *381*, 122668. [[CrossRef](#)]
47. Nguyen, T.P.T.; Yang, K.H.; Kim, M.H.; Hong, Y.S. Selective catalytic reduction of NO by NH₃ over Fe₂O₃-promoted V₂O₅/TiO₂-based catalysts with high Fe₂O₃-to-V₂O₅ ratios. *Catal. Today* **2020**. [[CrossRef](#)]
48. Zhu, N.; Shan, W.; Lian, Z.; Zhang, Y.; Liu, K.; He, H. A superior Fe-V-Ti catalyst with high activity and SO₂ resistance for the selective catalytic reduction of NO with NH₃. *J. Hazard. Mater.* **2019**, *382*, 120970. [[CrossRef](#)]
49. Wang, P.; Chen, S.; Gao, S.; Zhang, J.; Wang, H.; Wu, Z. Niobium oxide confined by ceria nanotubes as a novel SCR catalyst with excellent resistance to potassium, phosphorus, and lead. *Appl. Catal. B Environ.* **2018**, *231*, 299–309. [[CrossRef](#)]
50. Lian, Z.; Shan, W.; Zhang, Y.; Wang, M.; He, H. Morphology-dependent catalytic performance of NbO_x/CeO₂ catalysts for selective catalytic reduction of NO_x with NH₃. *Ind. Eng. Chem. Res.* **2018**, *57*, 12736–12741. [[CrossRef](#)]
51. Liu, F.; Asakura, K.; He, H.; Shan, W.; Shi, X.; Zhang, C. Influence of sulfation on iron titanate catalyst for the selective catalytic reduction of NO_x with NH₃. *Appl. Catal. B Environ.* **2011**, *103*, 369–377. [[CrossRef](#)]
52. Mendiola-Alvarez, S.Y.; Hernández-Ramírez, A.; Guzmán-Mar, J.L.; Maya-Treviño, M.L.; Caballero-Quintero, A.; Hinojosa-Reyes, L. A novel P-doped Fe₂O₃-TiO₂ mixed oxide: Synthesis, characterization and photocatalytic activity under visible radiation. *Catal. Today* **2019**, *328*, 91–98. [[CrossRef](#)]
53. Pu, Z.; Liu, Q.; Asiri, A.M.; Luo, Y.; Sun, X.; He, Y. 3D macroporous MoS₂ thin film: In situ hydrothermal preparation and application as a highly active hydrogen evolution electrocatalyst at all pH values. *Electrochim. Acta.* **2015**, *168*, 133–138. [[CrossRef](#)]
54. Hanawa, T.; Hiromoto, S.; Asami, K. Characterization of the surface oxide film of a Co-Cr-Mo alloy after being located in quasi-biological environments using XPS. *Appl. Surf. Sci.* **2001**, *183*, 68–75. [[CrossRef](#)]
55. Zhang, J.; Huang, Z.; Du, Y.; Wu, X.; Shen, H.; Jing, G. Alkali-poisoning-resistant Fe₂O₃/MoO₃/TiO₂ catalyst for the selective reduction of NO by NH₃: The role of the MoO₃ safety buffer in protecting surface active sites. *Environ. Sci. Technol.* **2020**, *54*, 595–603. [[CrossRef](#)] [[PubMed](#)]
56. France, L.J.; Li, W.; Zhang, Y.; Mu, W.; Chen, Z.; Shi, J.; Zeng, Q.; Li, X. A superior Fe-Zr mixed oxide catalyst for the simultaneous reduction of NO and SO₂ with CO. *Appl. Catal. B Environ.* **2020**, *269*, 118822. [[CrossRef](#)]
57. Zhang, Z.; Li, R.; Wang, M.; Li, Y.; Tong, Y.; Yang, P.; Zhu, Y. Two steps synthesis of CeTiO_x oxides nanotube catalyst: Enhanced activity, resistance of SO₂ and H₂O for low temperature NH₃-SCR of NO_x. *Appl. Catal. B Environ.* **2021**, *282*. [[CrossRef](#)]
58. Xu, Q.; Fang, Z.; Chen, Y.; Guo, Y.; Guo, Y.; Wang, L.; Wang, Y.; Zhang, J.; Zhan, W. Titania-samarium-manganese composite oxide for the low-temperature selective catalytic reduction of NO with NH₃. *Environ. Sci. Technol.* **2020**, *54*, 2530–2538. [[CrossRef](#)] [[PubMed](#)]
59. Han, L.; Gao, M.; Feng, C.; Shi, L.; Zhang, D. Fe₂O₃-CeO₂@Al₂O₃ nanoarrays on Al-mesh as SO₂-tolerant monolith catalysts for NO_x reduction by NH₃. *Environ. Sci. Technol.* **2019**, *53*, 5946–5956. [[CrossRef](#)]
60. Zhang, X.; Shen, Q.; He, C.; Ma, C.; Cheng, J.; Li, L.; Hao, Z. Investigation of selective catalytic reduction of N₂O by NH₃ over an Fe-mordenite catalyst: Reaction mechanism and O₂ effect. *ACS Catal.* **2012**, *2*, 512–520. [[CrossRef](#)]
61. Shu, Y.; Sun, H.; Quan, X.; Chen, S. Enhancement of catalytic activity over the iron-modified Ce/TiO₂ catalyst for selective catalytic reduction of NO_x with ammonia. *J. Phys. Chem. C* **2012**, *116*, 25319–25327. [[CrossRef](#)]
62. Zhu, B.; Zi, Z.; Sun, Y.; Fang, Q.; Xu, J.; Song, W.; Yu, H.; Liu, E. Enhancing low-temperature SCR de-NO_x and alkali metal poisoning resistance of a 3Mn10Fe/Ni catalyst by adding Co. *Catal. Sci. Technol.* **2019**, *9*, 3214–3225. [[CrossRef](#)]
63. Yang, J.; Ren, S.; Zhou, Y.; Su, Z.; Yao, L.; Cao, J.; Jiang, L.; Hu, G.; Kong, M.; Yang, J.; et al. In situ IR comparative study on N₂O formation pathways over different valence states manganese oxides catalysts during NH₃-SCR of NO. *Chem. Eng. J.* **2020**, *397*, 125446. [[CrossRef](#)]
64. Yang, S.; Wang, C.; Li, J.; Yan, N.; Ma, L.; Chang, H. Low temperature selective catalytic reduction of NO with NH₃ over Mn-Fe spinel: Performance, mechanism and kinetic study. *Appl. Catal. B Environ.* **2011**, *110*, 71–80. [[CrossRef](#)]
65. Lv, Y.; Yao, W.; Zong, R.; Zhu, Y. Fabrication of wide-range-visible photocatalyst Bi₂WO_{6-x} nanoplates via surface oxygen vacancies. *Sci. Rep.* **2016**, *6*, 19347. [[CrossRef](#)] [[PubMed](#)]
66. Li, K.; Chen, J.; Bai, B.; Zhao, S.; Hu, F.; Li, J. Bridging the reaction route of toluene total oxidation and the structure of ordered mesoporous Co₃O₄: The roles of surface sodium and adsorbed oxygen. *Catal. Today* **2017**, *297*, 173–181. [[CrossRef](#)]
67. Xu, L.; Niu, S.; Lu, C.; Zhang, Q.; Li, J. Influence of calcination temperature on Fe_{0.8}Mg_{0.2}O catalyst for selective catalytic reduction of NO with NH₃. *Fuel* **2018**, *219*, 248–258. [[CrossRef](#)]
68. Wu, S.; Zhang, L.; Wang, X.; Zou, W.; Cao, Y.; Sun, J.; Tang, C.; Gao, F.; Deng, Y.; Dong, L. Synthesis, characterization and catalytic performance of FeMnTiO_x mixed oxides catalyst prepared by a CTAB-assisted process for mid-low temperature NH₃-SCR. *Appl. Catal. A Gen.* **2015**, *505*, 235–242. [[CrossRef](#)]
69. Marberger, A.; Elsener, M.; Ferri, D.; Sagar, A.; Scherzmanz, K.; Krocher, O. Generation of NH₃ selective catalytic reduction active catalysts from decomposition of supported FeVO₄. *ACS Catal.* **2015**, *5*, 4180–4188. [[CrossRef](#)]
70. Xin, Y.; Li, H.; Zhang, N.; Li, Q.; Zhang, Z.; Cao, X.; Hu, P.; Zheng, L.; Anderson, J.A. Molecular-level insight into selective catalytic reduction of NO_x with NH₃ to N₂ over a highly efficient bifunctional Va-MnO_x catalyst at low temperature. *ACS Catal.* **2018**, *8*, 4937–4949. [[CrossRef](#)]